Glass Europe Vol. 2 (2024) 165-179
https://doi.org/10.52825/glass-europe.v2i.2538

Submitted: 14 Nov. 2024 | Accepted: 03 Dec. 2024 | Published: 17 Dec. 2024

Effect of Cation Exchange on the Kinetics of Thermal Amorphization of Zeolite X

Ayda Nemati Vesali Azar[1] and Lothar Wondraczek[1,2]

[1] Otto Schott Institute of Materials Research, University of Jena, Jena, Germany

[2] Center of Energy and Environmental Chemistry, University of Jena, Jena, Germany

*Correspondence: Lothar Wondraczek, lothar.wondraczek@uni-jena.de

Abstract. Thermal collapse of crystalline zeolites offers a way to obtain glasses in chemical regimes that are inaccessible by classical melt quenching. Thereby, the charge-balancing cations located within the zeolitic framework play an important role in determining structural stability and the dynamics of collapse. Here, we use ion exchange in aqueous solution to create a consistent variety of alkali, alkaline earth and transition-metal containing derivatives of the faujasitic Zeolite X. We subsequently explore the effect of cation species on the thermal stability and the collapse dynamics, revealing a systematic decrease of zeolite stability with increasing cation electronegativity, but a more complex correlation for the apparent activation energy of the collapse reaction.

Keywords: Thermal Amorphization, Amorphization Kinetics, Zeolite, Ion-Exchange

1. Introduction

Zeolitic aluminosilicates have a wide range of large-scale applications.[1], [2], [3] Many of these applications rely on the material's thermal stability: thermally-induced structural transitions have received renewed attention, in particular, when reactions of thermal switching and thermally-triggered host-guest interactions were discovered. The general zeolite framework comprises of corner-sharing $[SiO_4]^{4-}$ and $[AlO_4]^{5-}$ tetrahedra, charge-balanced by cations located within the network voids. When increasing the temperature, the initially porous structure collapses into an amorphous state that may subsequently recrystallize to a dense phase (such as carnegieite or nepheline). [4], [5], [6] The secondary crystallization reaction attracted some interest because it enables the production of ceramic materials (from natural zeolites) at significantly lower temperatures when compared to traditional ceramic forming techniques.[7], [8] Similarly, amorphization was discussed as a means to obtain otherwise inaccessible states of glass.[9], [10], [11] In particular, it was discovered that thermal or pressure-induced amorphization involves a polyamorphic transition from an initial, low-density amorphous phase (LDA) to a high-density amorphous phase (HDA). [12], [13], [14] A kinetic model was derived to explain the associated compressed exponential reaction kinetics on the basis of a two-step reaction model, starting from random, reversible structural distortions followed by diffusive, irreversible liberation (melting).[15], [16] The thermal window between structural collapse (amorphization) and secondary recrystallization sometimes enables quenching of the amorphous products into a glass-like state. This quenched state was found to resemble conventional aluminosilicate glasses, for example, exhibiting a mixed-alkali effect as a function of cation composition. However, the high framework-content of alumina usually precludes the production of chemically equivalent glasses by conventional melt-quenching; zeolite collapse therefore offers a route to

not only produce glass-like materials with unusual density, but also widens the range of accessible glass chemical compositions.

The charge-balancing cations play an important role in tuning the physicochemical properties of zeolites, including their mechanical and thermal stability. [16], [17] They can be exchanged with a wide variety of cations, whereby the degree of exchange indicates the extent to which the charge-balancing cations are replaced. This process can be performed at low temperatures by treating the material in aqueous solutions. In a previous study, we explored how the relative degree of ion exchange (IOX) affects the kinetics of amorphization, using a specific pair of alkali species (*i.e.*, K for Na).[16] We observed a turning point at an exchange degree of ~ 30%, at which a maximum occurred in the kinetic stability of the zeolite framework. On this line, we now consider the effect of cation species when exchanged to a degree near this maximum. For this, three groups of IOX materials were studied, *i.e.*, zeolite X in which sodium is exchanged by other alkali, alkaline earth and transition metals ions, respectively. Non-isothermal collapse of these materials was examined using X-ray diffraction (XRD), differential scanning calorimetry coupled with thermo-gravimetric analysis (DSC-TGA), scanning electron microscopy (SEM) and Raman spectroscopy in the context of forming glasses with unusual chemical composition.

2. Methods

2.1 IOX procedure

Zeolite X ($Na_2O.Al_2O_3.mSiO_2$ with $m \leq 2.35$, termed NaX) was supplied by Chemiewerk Bad Köstritz, Germany. IOX was used to synthesize three distinct sets of zeolite X derivatives. The initial group (alkali exchange) involved the exchange of sodium ions from the parent NaX for lithium (Li) and potassium (K). Further groups were prepared by substituting sodium with magnesium (Mg), calcium (Ca), strontium (Sr), and cobalt (Co) or zinc (Zn), respectively. The IOX procedure was designed to yield an intermediate IOX degree of 25-40 % in terms of the cation concentration of the target species relative to sodium. For this, 5 g of the parent NaX powder were immersed in a 0.1 M aqueous solution of the respective chloride compounds, MCl or MCl_2 (M: target cation), at a temperature of approximately 55°C for a duration of 30 minutes. Following partial IOX, the obtained zeolite powder was recovered by vacuum filtration and washed thoroughly in 250 ml of deionized water at room temperature. Final samples were dried overnight at 80°C and stored in desiccators at room temperature for further use.

2.2 IOX Characterization techniques

Powder XRD patterns were collected using a Rigaku Smartlab diffractometer with Cu-Kα1 radiation (1.54059 Å) in Bragg-Brentano geometry. The experimental set-up included a Hypix-3000 horizontal detector, a 5 mm length-limiting slit, a 5° Soller slit, a Kβ filter, and a beam shutter. The X-ray tube operated at 50 mA current and 40 kV voltage. Diffraction patterns of the samples were collected over the 2θ range of 5-45°, with a step size of 0.01° and a scan speed of 5° per minute.

The thermal behavior of the samples was analyzed by differential scanning calorimetry coupled with thermal gravimetric analysis (DSC-TGA, Netzsch STA 449 F1). For this, 15 mg of each sample were loaded into a platinum crucible and heated from room temperature to 1200 °C with heating rate of 10 K/min under 20 ml/min N_2 flow.

Particle size, morphology, and elemental composition of each sample were analyzed through scanning electron microscopy (SEM) with a JSM-7001F microscope (Jeol, Japan), equipped with an energy-dispersive X-ray spectrometer (EDX).

Raman spectra were acquired over the frequency range of 200 – 900 cm^{-1} using a Renishaw inVia Raman microscope with an excitation wavelength of 633 nm. Prior to spectrum acquisition, the surface of the powder samples was flattened by mild compression. Each spectrum was generated from an average of three accumulations, with a scan acquisition time of 180 s per scan.

Non-isothermal XRD patterns were collected in time intervals of 60 s per pattern over the 2θ range of 5-12° with a Rigaku Smartlab equipped with an HTK1200N (Anton Paar) heating stage. Data were collected from room temperature to 1100 °C during continuous heating at rates of 5, 10 and 20 K/min with a step size of 0.01° and a scan speed of 50 °/min.

3. Result and discussion

3.1 Samples characterization

The nature of the charge-balancing cations influences the physicochemical characteristics of zeolites.[18] In order to investigate the impact of various cations on the amorphization kinetics of zeolite X, we synthesized a set of samples containing various types of cations. Specifically, we examined K^+, Na^+, and Li^+ ions from the alkali metal group, and Sr^{2+}, Ca^{2+}, and Mg^{2+} ions from the alkaline earth metal group. We additionally synthesized samples containing Co^{2+} and Zn^{2+} to represent the effect of transition metal ions on amorphization kinetics. According to previous observations, a higher degree of IOX reduces the overall framework stability by Si-O-Si and Si-O-Al bond opening reactions, which in turn affect the amorphization process.[17], [19] To avoid framework distortion during IOX procedure we therefore limited the overall degree of IOX to a maximum of 40 %.

The elemental composition of the samples was determined using EDX analysis, from which the degree of IOX was obtained as the ratio of the target metal (M) to the sodium content observed in four separate EDX measurements on each sample.

Table 1. *Atomic percentage of Na and target metal cation (M) for each sample.*

	NaX	**NaKX**	**NaMgX**	**NaCaX**	**NaSrX**	**NaCoX**	**NaZnX**
Na	21	18	14	16	15	17	15
M	0	5	5	6	11	6	5
M/(Na+M) (%)	0	22.8	25.1	26.1	42.2	26.4	25.7

Table 1 shows the atomic percentage of Na and M elements obtained by EDX, along with the corresponding degrees of exchange. Apart from NaSrX, all samples exhibit IOX degrees ranging from 20% to 25%. The elevated degree observed in NaSrX may be attributed to the electrochemical properties of strontium.[20] It is noteworthy that the utilized technique for assessing the elemental composition of samples (EDX) was unable to quantify the lithium content of the NaLiX sample. However, considering the uniformity in synthesis methodology applied to this sample, we predict an IOX degree of less than 40% for NaLiX, too.

The crystal morphology of faujasitic zeolite is octahedral, ideally with eight equilateral triangles; it is affected by a range of parameters, *e.g.*, crystal growth rate, presence of impurities, synthesis temperature, and post-processing.[21] SEM micrographs of the parent NaX and the various IOX samples are shown in Figure 1.

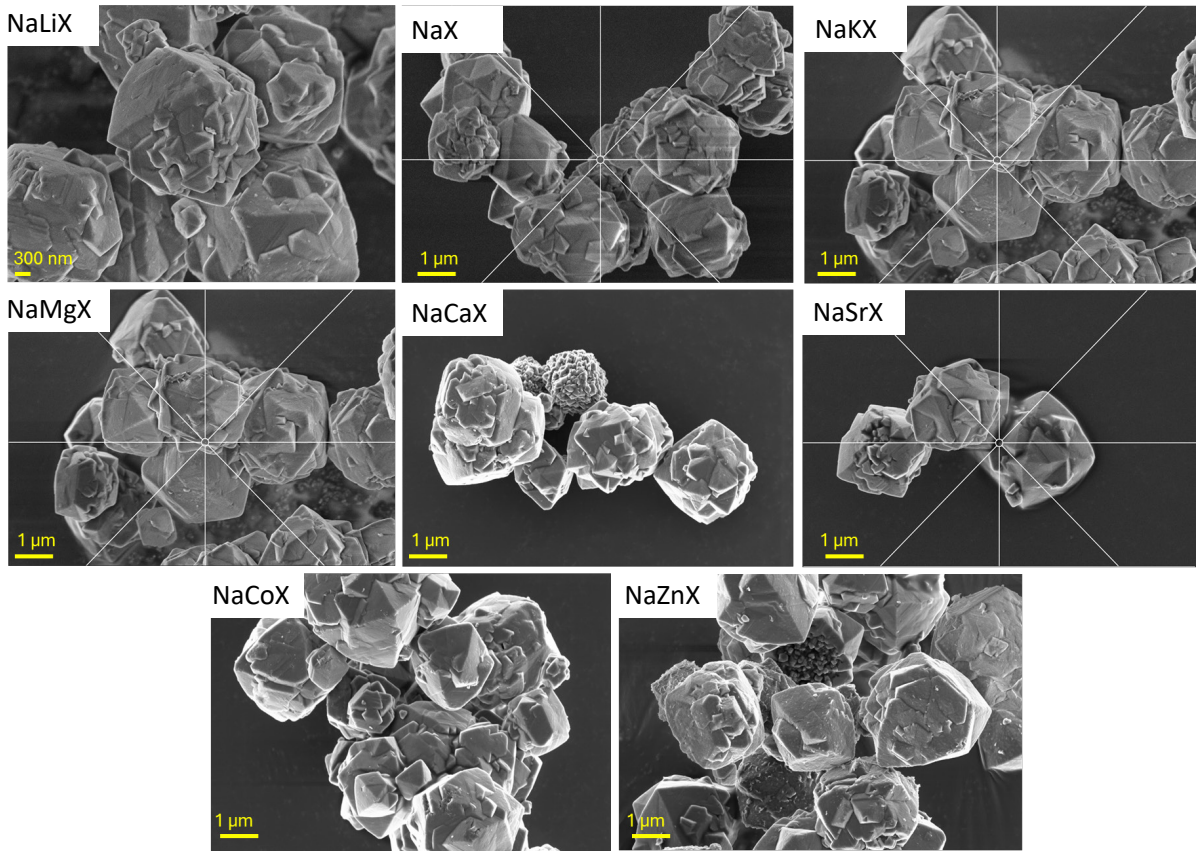

Figure 1. *SEM micrographs of parent Zeolite X (NaX) and IOX materials as labelled.*

Most importantly, this observation revealed that the crystal morphology of the samples was largely unaffected by IOX, except for the NaCoX material. In this latter case, the previously sharp edges of the zeolite octahedra turned into more rounded shapes, and the surface roughness of the individual crystals appeared to have increased, indicating the presence of surface deposits and/or selective etching as a result of IOX treatment.[22]

As observed previously, the IOX procedure may cause rearrangement of atoms within the zeolite lattice, leading to a severe loss of zeolite crystallinity.[23] We therefore combined XRD and Raman in order to further characterize the structure of the materials obtained after IOX. Figure 2 shows XRD patterns of parent and IOX zeolite X materials. As an overall observation, the crystallinity of all samples remained intact following the IOX procedure; crystal structures of all samples closely match the diffraction pattern of the parent NaX sample. Comparison of the maximum peak positions revealed a slight shift towards lower 2θ values with increasing cation size within the alkali and alkaline earth metal groups. This shift occurs because of network expansion with increasing size of the charge-balancing cations. For the same reason, the diffraction peaks for NaCoX and NaZnX samples (with transition metal ions having lower radius as compared to Na^+) shifted to slightly higher values of 2θ (see insets of Figure 2).

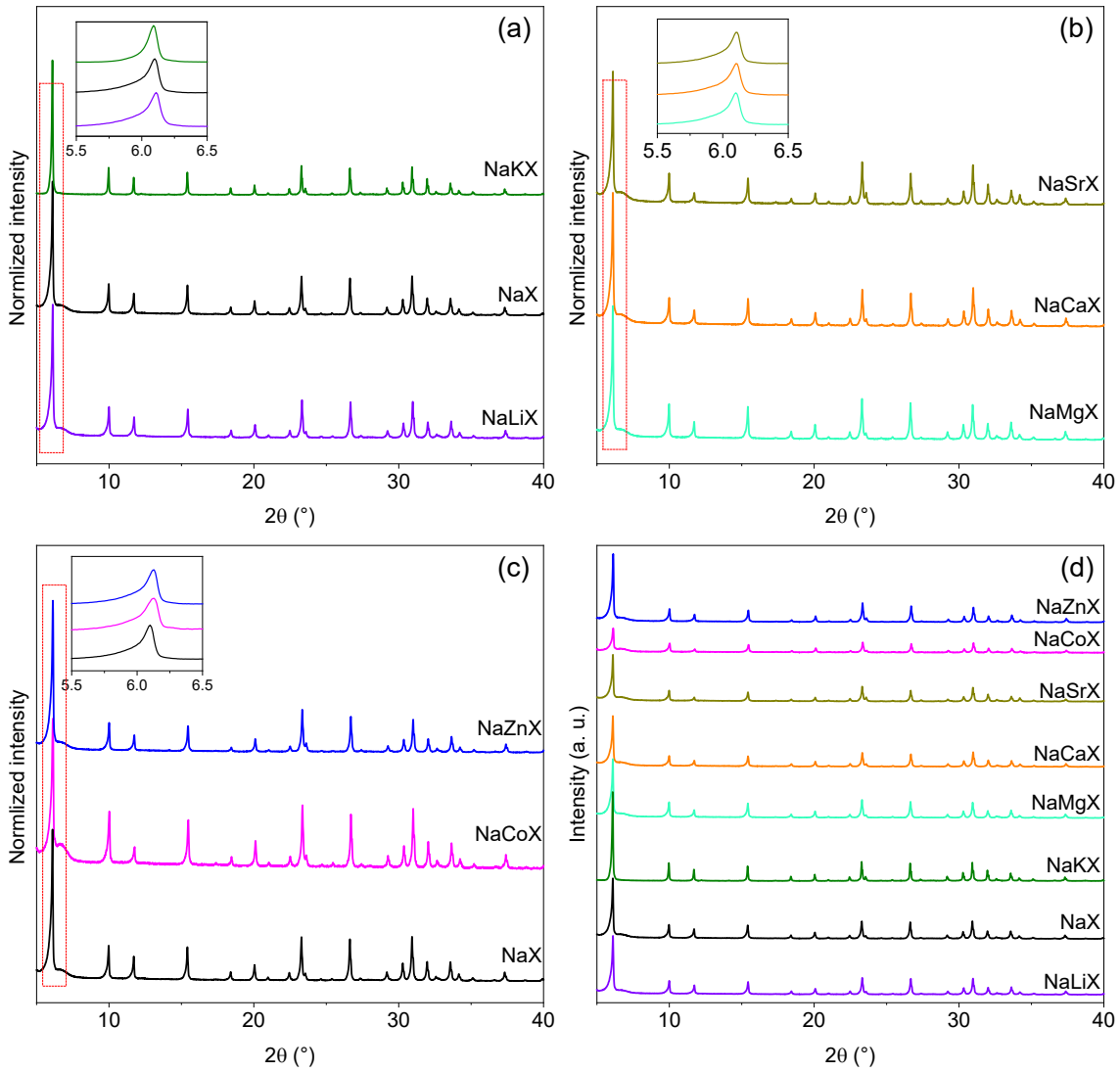

Figure 2. *XRD diffraction patterns for zeolite IOX derivatives using alkali (a), alkaline earth (b), and transition metal cations (c) for IOX.*

Table 2*. Atomic radius* r_{atom}, *ionic radius* r_{ion} *and electronegativity* χ *of charge-balancing ions used for IOX.[24]*

	Li	Na	K	Mg	Ca	Sr	Co	Zn
r_{atom} (Å)	1.34	1.54	1.96	1.30	1.74	1.92	1.92	1.39
r_{ion} (Å)	0.68	0.97	1.33	0.66	0.99	1.13	0.82	0.83
χ	0.98	0.93	0.82	1.31	1.00	0.95	1.88	1.65

Table 2 summarizes the atomic radii r_{atom}, the ionic radii r_{ion}, and the electronegativity values χ of the metal species used in this study.[24]

As further seen in Figure 2, the intensity of the diffraction peaks did not change significantly for all samples except NaCoX. Earlier studies showed that replacing a monovalent charge balancing cation with divalent cations can perturbs the oxygen atom arrangement, leading to partial deformation of the zeolite framework even at lower IOX degree.[25] This seems to be

the case for NaCoX, but less so for the other divalent IOX species; it is in agreement with the previous SEM observations.

The XRD observations were confirmed by Raman spectroscopy. According to literature, Raman bands at around 470-500, 290-410, and 220- 280 cm^{-1} are assigned to the bending modes of 4-, 6- and 8- membered rings of aluminosilicate zeolites, respectively.[26] Figure 3 shows Raman spectra of the three sets of samples, together with the NaX reference spectrum. Zeolite X with alkali and alkaline earth cations as charge balancing species (Figure 3 (a), (b)) showed almost no change in the positions of Raman bands. This proves that the framework of the samples stayed intact with minimal distortion after the IOX process. However, the presence of transition metals in the framework influenced the Raman spectrum, especially in NaCoX. Zeolite X has a Raman band around 460 cm^{-1} which is assigned to internal vibrations of tetrahedra (TO_4) within the framework. As seen from Figure 3(c), incorporation of transition metals led to a significant change of this vibrational band; the Raman band at 460 cm^{-1} seems to merge with the dominant band near 514 cm^{-1} in these samples. In addition, this latter band blue-shifted to 535 cm^{-1} in NaCoX, while it slightly red-shifted in NaZnX. This suggests T-O-T bonding within 4-membered rings became stronger by introducing Co^{2+} cations, and that at the same time, IOX changed the local charge environment. The Raman band at 382 cm^{-1} is not detectable for NaCoX and the intensity of Raman band at 292 cm^{-1} decreased drastically. Apparently, the cobalt cations accumulate around the 6-membered ring, and this accumulation changes the polarizability of the zeolite framework.[27] Finally, new Raman bands arose in this sample, i.e., at 327 $cm^{-1}$and 670 cm^{-1}. They are assigned to vibrational modes of Co–O bonds.[28], [29], [30]

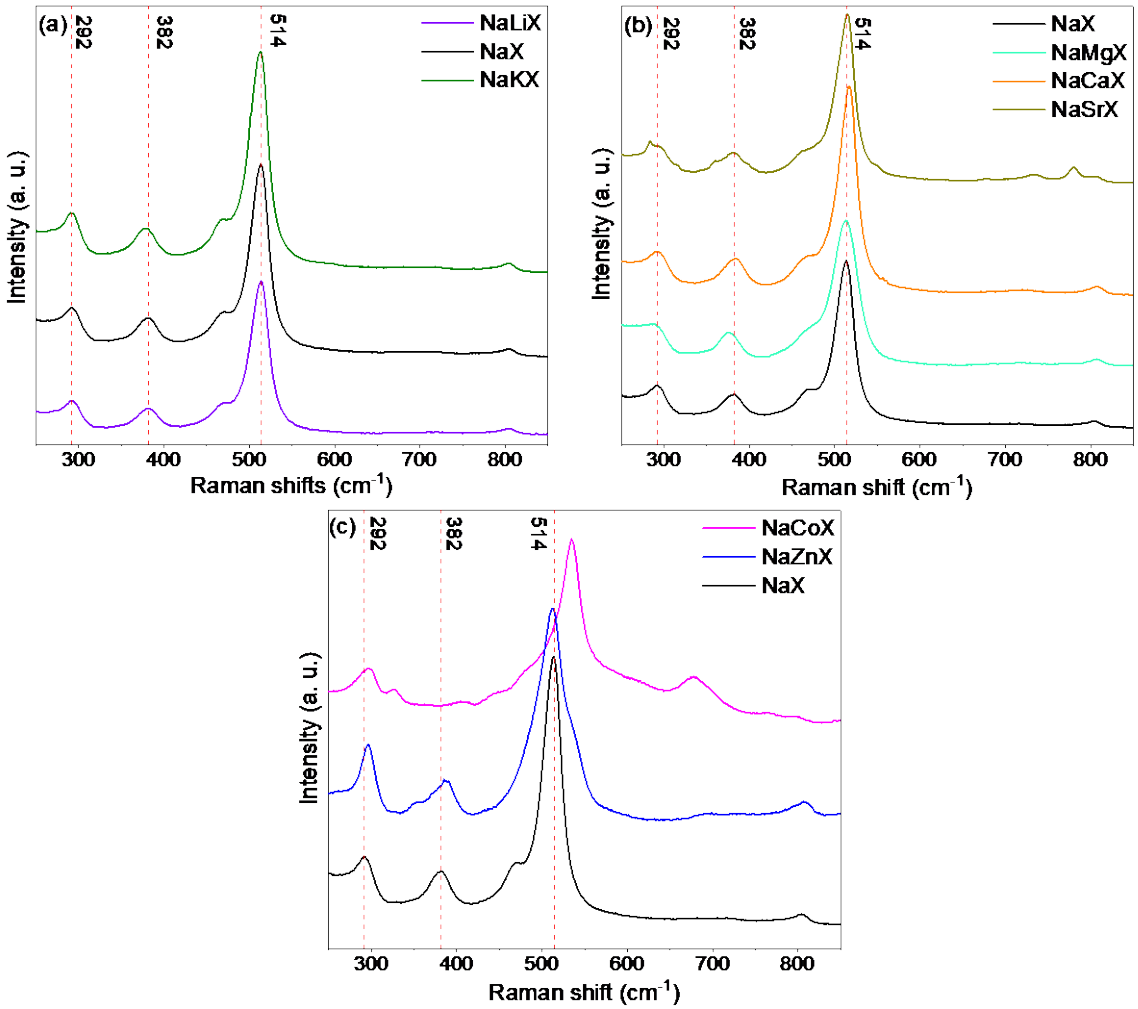

Figure 3. *Raman spectra for parent zeolite X (NaX) and alkali (a), alkaline earth(b), and transition(c) metal IOX samples (as labelled). The dashed lines are to mark prominent Raman bands of the parent zeolite X (see text for details)*

To investigate the thermal behavior of IOX samples, non-isothermal DSC scans were collected up to 1200 °C on all samples, using an identical heating rate of 10 °C/min. As shown in Figure 4(a), we introduced a dehydration step at 250 °C for 10 min to ensure that all physically adsorbed water was removed prior to further DSC scanning across the thermal transitions. At temperatures above 800 °C, distinct transitions occur in the parent NaX and all IOX samples, with the specific transition temperatures being dependent on the IOX species. The first exothermic transition is the thermally induced amorphization; the subsequent second and third peaks are due to recrystallization of carnegieite and nepheline, respectively.[6], [31] In the following analysis, we will focus exclusively on the first reaction, taken as the amorphization step, however, we also detected a clear change in the recrystallization temperatures following IOX (Figures 4(b-d)).

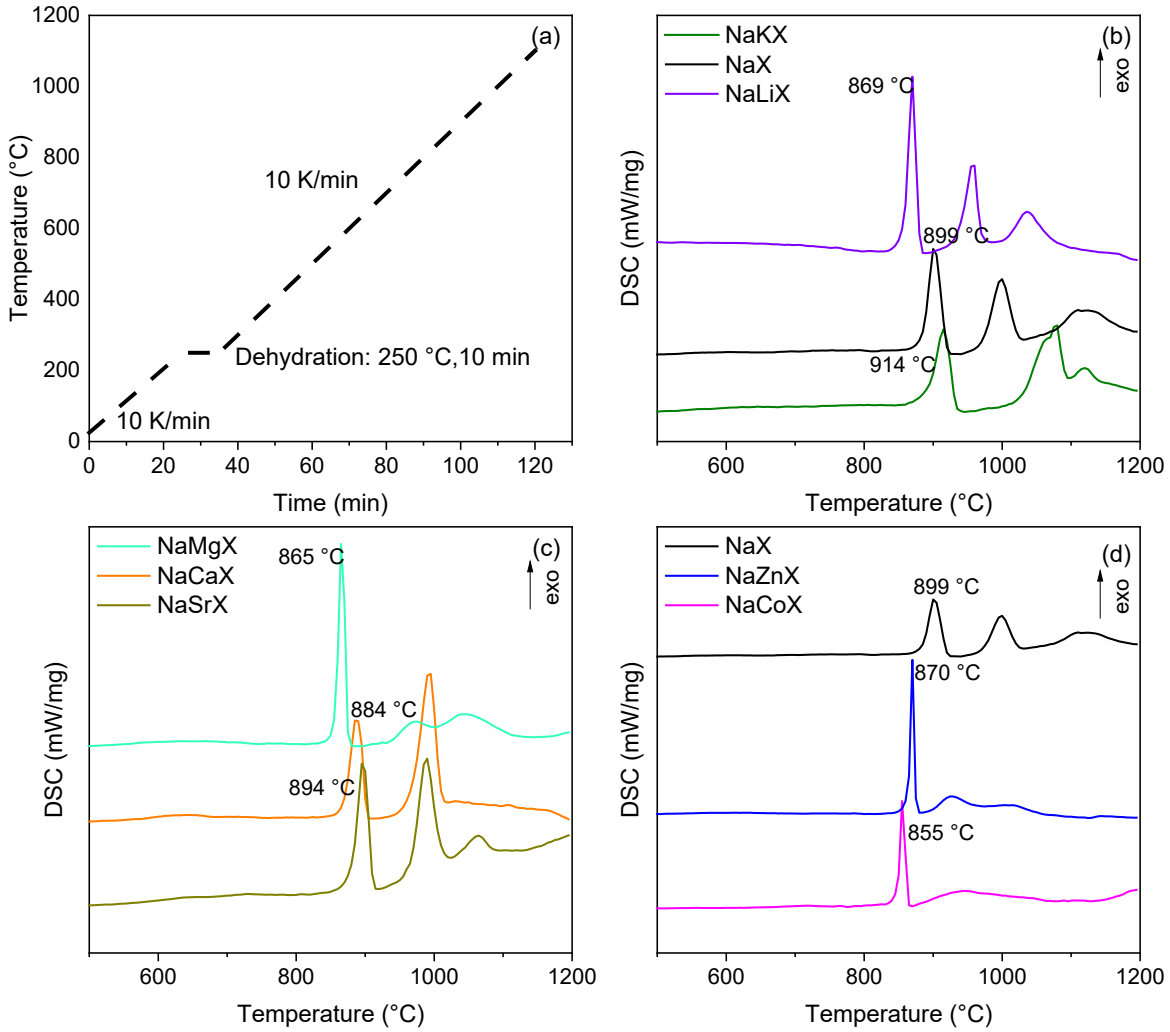

Figure 4. *Temperature profile used for non-isothermal DSC (a), and DSC scans of alkali (b) alkaline earth (b), and transition metal IOX zeolite X obtained at a heating rate of 10 K/min.*

For the alkali metal IOX (Figure 4(b)), the thermally induced amorphization temperature follows the sequence of ionic radii; it increases from Li^+ to K^+. This indicates that the presence of larger cations within the supercages hinders ion diffusion, and thus enhances the thermal stability of the zeolite framework against thermal collapse. The larger ions exert a lower field strength, what probably further stabilizes the T-O-T bonding and the zeolite framework stability at moderate IOX degrees. We observed the same trend for alkaline earth metals (Figure 4 (c)), for which the amorphization temperature increased from NaMgX (865 °C) to NaCaX (884 °C), and further to NaSrX (894 °C). Although we see a similar trend for both alkali and alkaline earth IOX, there is an absolute shift in the thermal amorphization temperature in that the alkaline earth IOX materials are generally more stable.

Figure 4(d) shows the thermal amorphization of the transition metal IOX samples relative to that of the NaX parent. Due to the significant difference in electronegativity of the transition metals compared to that of alkali or alkaline earth metals, the electronic environment of the metal-oxygen sites varies significantly between these two groups. This is in line with our results from Raman spectroscopy analysis where we observed Raman band shifts and even the appearance of new bands assigned to metal-oxygen bonds for the transition metal IOX materials. In this case, IOX results in structural and chemical alterations within the zeolite framework, which is also reflected in the thermally induced phase transitions. The thermal amorphization temperature is lower for NaZnX and NaCoX as compared to that of NaX, with the lowest temperature being that of NaCoX. The electronic configuration and the higher electronegativity of

Co (Co^{2+} and Co^{3+}, $[Ar]3d^7$ and $[Ar]3d^6$) as compared to that of Zn^{2+} ($[Ar]3d^{10}$) cause a more distorted electron density and higher electronic interaction for the former, leading to lower thermal amorphization temperature, regardless even of the specific oxidation state of Co.

3.2 Non-isothermal amorphization kinetics

The structural collapse of the samples was monitored using non-isothermal X-ray diffraction (XRD) with heating rates of 5, 10, and 20 K/min. In this, we considered the area under the most intense XRD diffraction peak at 6° as an internal variable to quantify the progress of the collapse reaction. [15], [16]

The reaction progress for alkali, alkaline earth, and transition metal zeolite X derivatives is depicted in Figure 5 (a)-(c), respectively. Considering the known collapse mechanism of zeolite X, as the temperature rises, we can clearly observe a decay of the normalized area under the most intense diffraction peak. In order to quantify the reaction progress from non-isothermal data, we use a previous empirical model of characteristic temperatures.[12], [16] In this, the progress accelerates at a temperature T_1 (onset temperature of amorphization), reaches a maximum conversion rate at T_A, and decelerates at T_2 (onset of reaction cessation); T_A is the inflection point of the time correlation function. For all samples, the amorphization process accelerates at temperatures above 700 °C, and transitions into a fully amorphous stage at temperatures below 900 °C. Larger symbols in Figure 5 (a)-(c) denote T_A for each sample. It is evident that with an increase in the ionic radius of charge-balancing cations within each group of samples, the maximum conversion rate shifts to higher temperatures. The zeolite X tends to initially exchange cations which are located within supercages, in particular, at lower degrees of IOX such as applied in the present study. As noted before, when the size of the charge-balancing cation increases, cations become less mobile by diffusion, thus contributing to enhanced stability of the framework.[32]

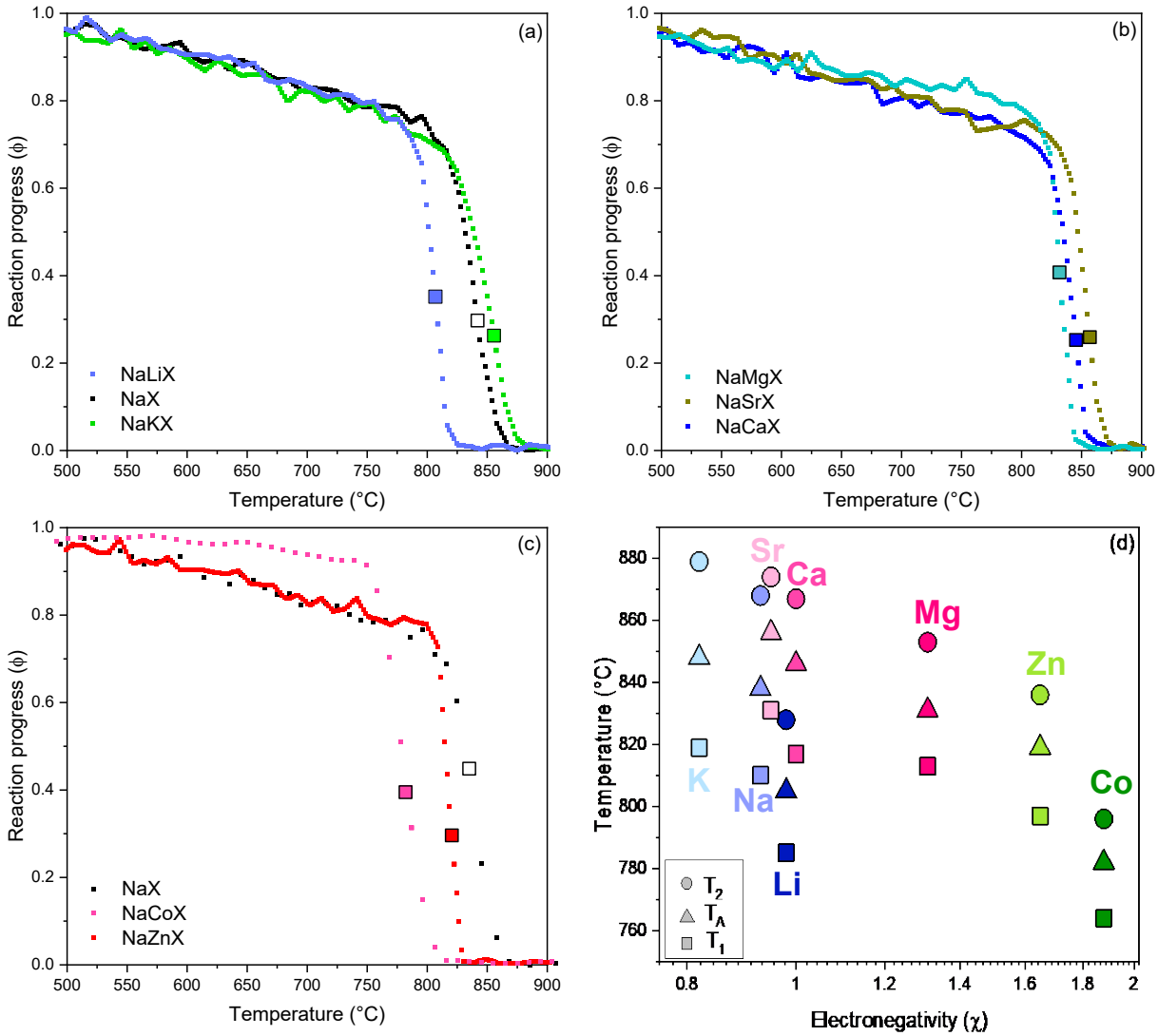

Figure 5. *Zeolite collapse reaction progress ϕ for alkali (a), alkaline earth (b) and transition metal (c) IOX materials derived from non-isothermal XRD patterns with heating rates of 10 K/min. (d) Transition temperatures of T1, T2, and TA.*

Figure 5 (d) shows the empirically derived characteristic temperatures, revealing a visible correlation between electronegativity and collapse temperature across sample groups. Notably, the amorphization temperature for NaLiX is observed at 805°C, while this value increases to 848°C for NaKX. Similarly, NaMgX exhibits an amorphization temperature of 831°C, which rises to 856°C for NaSrX.

A consistent pattern emerges when comparing T_A of IOX material within the same subgroup. For instance, NaMgX, which exhibits a greater affinity towards framework oxygens, exhibits a lower collapse temperature relative to NaLiX. However, this trend diverges with NaSrX, potentially because of this particular sample's higher IOX degree. As shown in earlies studies, increased IOX degree induces perturbations within the framework, consequently influencing the thermal stability of the zeolite and trading-off on potential increases in T_A.

In line with the observations made by DSC, zeolite X incorporating Co as charge balancing cation exhibits notably reduced thermal stability. Specifically, NaCoX, featuring the highest electronegativity and smallest ionic radius of the studied IOX species, has an onset of melting already at approximately 760°C, a reduction of 50°C compared to the NaX parent. This aligns well with our observation regarding the red shift of the Raman band. We distinctly noted a

decrease in bond strength within the 4-membered ring upon the incorporation of the cobalt cation.

According to an empirical equation introduced by Greaves *et al*., the collapse reaction time τ_A is directly related to both T_1 and T_2, while being inversely correlated with the applied heating rate during non-isothermal observation of the collapse reaction,[12]

$$\tau_A = \frac{(T_2 - T_1)}{q} \quad (1)$$

Using Eq. 1, the apparent amorphization time τ_A was calculated for all samples (Table 3).

Table 3. *Amorphization time calculated based on T1 and T2.*

Sample	Na-LiX	NaX	NaKX	NaMgX	NaCaX	NaSrX	NaCoX	NaZnX
Amorphization time, τ_A (s)	258	348	360	240	300	258	192	234

Here, NaKX and NaCaX exhibit not only the highest thermal stability, but also the longest amorphization times, whereas NaCoX, with a collapse time of 192 s, undergoes the fastest amorphization process. The overall trend in amorphization time corresponds to that of amorphization temperature within each group of samples.

Finally, we used Kissinger's equation in order to calculated the apparent activation energy of the collapse reaction[33], E_a,

$$\ln\left(\frac{q}{T_A^2}\right) = -\frac{E_a}{RT_A}, \quad (2)$$

Here, R and q denote the universal gas constant, and the heating rate employed during non-isothermal analysis. Figure 6 (a)-(c) shows linearized Kissinger plots derived from non-isothermal XRD at heating rates of 5, 10, and 20 K/min. The slope of these plots corresponds to $\frac{E_a}{R}$; the calculated values of E_a are provided in Figure 6 (d). According to these data, the alkali metal ions exhibit the lowest electronegativities and activation energies (550–650 kJ/mol). In contrast, the IOX derivatives containing alkaline earth species require higher activation energy to initiate structural collapse, what is in accordance with the interpretations of reduced diffusive mobility. We infer that alkaline earth ions exert stronger electrostatic interactions with the zeolite framework, resulting in a higher apparent activation energy, within the limits of interpretability of this metric. Samples containing transition metals, which exhibit the highest electronegativity among the groups studied, have apparent activation energies intermediate between those of the alkali and alkaline earth IOX materials. While higher electronegativity is typically associated with an expectation of higher apparent activation energy, our Raman characterization revealed that the incorporation of transition metals induces higher polarizability. These changes likely contribute to the observed reduction in apparent activation energy for IOX derivatives containing transition metals.

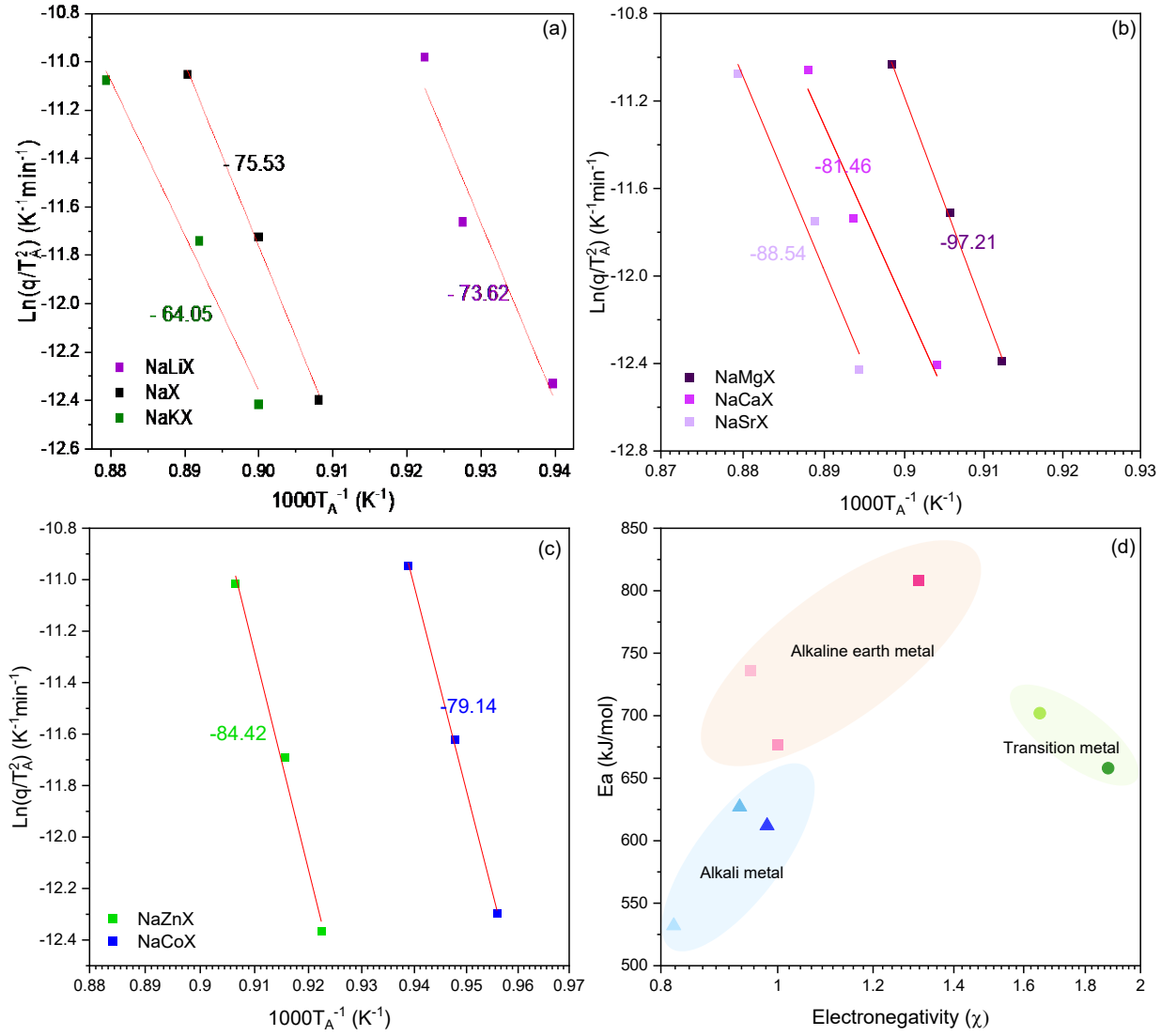

Figure 1. *Linearized Kissinger plot for alkali (a), alkaline earth (b), and transition metal (c) IOX materials. (d) Apparent activation energy calculated using on non-isothermal XRD.*

4. Conclusion

To isolate the effect of charge-balancing cations on kinetics of zeolite amorphization, we synthesized samples with low IOX degrees (<40%) using three groups of cation species for ion exchange: alkali (Li, Na, K), alkaline earth (Mg, Ca, Sr), and transition metal (Co and Zn). By this selection, structural changes leading to altered amorphization kinetics were investigated. In general, maintaining a low degree of IOX eliminated structural distortion of the zeolitic backbone framework during the IOX procedure. This enabled examination of the sole effect of charge balancing cation species on the kinetics of thermal collapse. As major factors influencing the amorphization reaction, we find that the size and electron configuration of the cation determine the structural and thermal stability of zeolite X. Cations with higher electronegativity form stronger bonds with tetrahedral bridging oxygen, leading to local instability to the framework and consequently reducing the amorphization temperature. Furthermore, our findings indicate that the presence of larger cations within the supercage in samples with lower IOX degrees, which are difficult to relocate and diffuse through the smaller pores of the framework, results in an increase in the amorphization temperature.

Data availability statement

Data of presented results can be provided upon request.

Author contributions

LW conceived of the project. ANVA conducted all experiments and collected collapse data. Both authors jointly evaluated the data, wrote and revised the manuscript.

Competing interests

The authors declare that they have no competing interests.

Acknowledgement

This project received funding through Germany´s Excellence Strategy (EXC 2051, project ID 390713860) and from the Carl Zeiss Foundation (Durchbrüche 2019).

References

[1] G. K. Li *et al.*, “Temperature-regulated guest admission and release in microporous materials,” *Nature Communications*, vol. 8, pp. 1–9, 2017, doi: 10.1038/ncomms15777.

[2] K. Narang, K. Fodor, A. Kaiser, and F. Akhtar, “Optimized cesium and potassium ion-exchanged zeolites A and X granules for biogas upgrading,” *RSC Advances*, vol. 8, no. 65, pp. 37277–37285, 2018, doi: 10.1039/c8ra08004f.

[3] J. E. Readman, C. P. Grey, M. Ziliox, L. M. Bull, and A. Samoson, “Comparison of the 17O NMR spectra of zeolites LTA and LSX,” *Solid State Nuclear Magnetic Resonance*, vol. 26, no. 3-4 SPEC. ISS., pp. 153–159, 2004, doi: 10.1016/j.ssnmr.2004.03.004.

[4] A. M. Beale, G. Sankar, D. G. Nicholson, and W. Van Beek, “In situ study of the crystallisation of nano-sized zinc and cobalt aluminate spinel catalysts from ion-exchanged zeolite precursors,” *Physica Scripta T*, vol. T115, pp. 678–680, 2005, doi: 10.1238/Physica.Topical.115a00678.

[5] L. M. Colyer, G. N. Greaves, S. W. Carr, and K. K. Fox, “Collapse and recrystallization processes in zinc-exchanged zeolite-A: A combined x-ray diffraction, XAFS, and NMR study,” *Journal of Physical Chemistry B*, vol. 101, no. 48, pp. 10105–10114, 1997, doi: 10.1021/jp9718008.

[6] T. Palenta, S. Fuhrmann, G. N. Greaves, W. Schwieger, and L. Wondraczek, “Thermal collapse and hierarchy of polymorphs in a faujasite-type zeolite and its analogous melt-quenched glass,” *Journal of Chemical Physics*, vol. 142, no. 8, 2015, doi: 10.1063/1.4913240.

[7] S. Ronchetti *et al.*, “Study of the thermal transformations of Co- and Fe-exchanged zeolites A and X by ‘in situ’ XRD under reducing atmosphere,” *Materials Research Bulletin*, vol. 45, no. 6, pp. 744–750, 2010, doi: 10.1016/j.materresbull.2010.02.006.

[8] S. Chen, J. Popovich, N. Iannuzo, S. E. Haydel, and D. K. Seo, “Silver-Ion-Exchanged Nanostructured Zeolite X as Antibacterial Agent with Superior Ion Release Kinetics and Efficacy against Methicillin-Resistant Staphylococcus aureus,” *ACS Applied Materials and Interfaces*, vol. 9, no. 45, pp. 39271–39282, 2017, doi: 10.1021/acsami.7b15001.

[9] L. Wondraczek *et al.*, “Thermal collapse of SAPO-34 molecular sieve towards a perfect glass,” *Journal of Non-Crystalline Solids*, vol. 360, no. 1, pp. 36–40, 2013, doi: 10.1016/j.jnoncrysol.2012.10.001.

[10] X. Li *et al.*, “Stress-tunable abilities of glass forming and mechanical amorphization,” *Acta Materialia*, vol. 277, no. June, p. 120218, 2024, doi: 10.1016/j.actamat.2024.120218.

[11] A. Navrotsky, “Ordered, disordered, collapsed,” *Nature*, vol. 2, pp. 571–572, 2003.

[12] G. N. Greaves *et al.*, “The rheology of collapsing zeolites amorphized by temperature and pressure,” *Nature Materials*, vol. 2, no. 9, pp. 622–629, 2003, doi: 10.1038/nmat963.
[13] G. N. Greaves, F. Meneau, F. Kargl, D. Ward, P. Holliman, and F. Albergamo, “Zeolite collapse and polyamorphism,” *Journal of Physics: Condensed Matter*, vol. 19, no. 41, p. 415102, 2007, doi: 10.1088/0953-8984/19/41/415102.
[14] G. N. Greaves, F. Meneau, and G. Sankar, “SAXS/WAXS and XAFS studies of zeolite stability,” *Nuclear Instruments and Methods in Physics Research, Section B: Beam Interactions with Materials and Atoms*, vol. 199, pp. 98–105, 2003, doi: 10.1016/S0168-583X(02)01599-9.
[15] L. Wondraczek *et al.*, “Kinetics of Decelerated Melting,” *Advanced Science*, vol. 5, no. 5, pp. 1–8, 2018, doi: 10.1002/advs.201700850.
[16] A. Nemati, V. Azar, A. Duval, and L. Wondraczek, “Mixed-alkali effect in the thermal collapse and melting kinetics of Zeolite X,” no. September, pp. 1–11, 2024, doi: 10.1111/jace.20185.
[17] C. Kosanović, A. C̆iz̆mek, B. Subotić, I. S̆mit, M. Stubic̆ar, and A. Tonejc, “Mechanochemistry of zeolites. Part 4: Influence of cations on the rate of amorphization of zeolite A by ball milling,” *Zeolites*, vol. 15, no. 7, pp. 632–636, 1995, doi: 10.1016/0144-2449(95)00036-6.
[18] U. D. Joshi *et al.*, “Influence of the size of extraframework monovalent cations in X-type zeolite on their thermal behavior,” *Thermochimica Acta*, vol. 387, no. 2, pp. 121–130, 2002, doi: 10.1016/S0040-6031(01)00840-1.
[19] C. Kosanović *et al.*, “Mechanochemistry of zeolites: Part 1. Amorphization of zeolites A and X and synthetic mordenite by ball milling,” *Zeolites*, vol. 13, no. 4, pp. 261–268, 1993, doi: 10.1016/0144-2449(93)90004-M.
[20] L. A. Freeman, J. E. Walley, and R. J. Gilliard, “Synthesis and reactivity of low-oxidation-state alkaline earth metal complexes,” *Nature Synthesis*, vol. 1, no. 6, pp. 439–448, 2022, doi: 10.1038/s44160-022-00077-6.
[21] H. J. Lee, Y. M. Kim, O. S. Kweon, and I. J. Kim, “Structural and morphological transformation of NaX zeolite crystals at high temperature,” *Journal of the European Ceramic Society*, vol. 27, no. 2–3, pp. 561–564, 2007, doi: 10.1016/j.jeurceramsoc.2006.04.156.
[22] A. N. V. Azar, A. Duval, F. Langenhorst, and L. Wondraczek, “Amorphization-controlled ion release of cobalt-exchanged zeolite X,” *Journal of the American Ceramic Society*, vol. 107, no. 10, pp. 6607–6618, 2024, doi: 10.1111/jace.19948.
[23] H. Qu, Y. Ma, B. Li, and L. Wang, “Hierarchical zeolites: synthesis, structural control, and catalytic applications,” *Emergent Materials*, vol. 3, no. 3, pp. 225–245, 2020, doi: 10.1007/s42247-020-00088-z.
[24] R. D. Shannon, “Revised effective ionic radii and systematic studies of interatomic distances in halides and chalcogenides,” *Acta Cryst A*, vol. 32, no. 5, pp. 751–767, Sep. 1976, doi: 10.1107/S0567739476001551.
[25] C. R. Technol, “Modified by Successive Ion Exchange,” 1993.
[26] Y. Yu, G. Xiong, C. Li, and F. S. Xiao, “Characterization of aluminosilicate zeolites by UV Raman spectroscopy,” *Microporous and Mesoporous Materials*, vol. 46, no. 1, pp. 23–34, 2001, doi: 10.1016/S1387-1811(01)00271-2.
[27] H. Sanaeepur, A. Kargari, B. Nasernejad, A. Ebadi Amooghin, and M. Omidkhah, “A novel Co2+ exchanged zeolite Y/cellulose acetate mixed matrix membrane for CO2/N2 separation,” *Journal of the Taiwan Institute of Chemical Engineers*, vol. 60, pp. 403–413, 2016, doi: 10.1016/j.jtice.2015.10.042.
[28] A. A. Verberckmoes, B. M. Weckhuysen, J. Pelgrims, and R. A. Schoonheydt, “Diffuse reflectance spectroscopy of dehydrated cobalt-exchanged faujasite-type zeolites: A new method for Co2+ siting,” *Journal of Physical Chemistry*, vol. 99, no. 41, pp. 15222–15228, 1995, doi: 10.1021/j100041a043.
[29] M. Christy *et al.*, “Lithium insertion behavior of nanoscopic Co3O4 prepared with avian Egg membrane as a template,” *Bulletin of the Korean Chemical Society*, vol. 32, no. 4, pp. 1204–1208, 2011, doi: 10.5012/bkcs.2011.32.4.1204.

[30] M. Król, W. Mozgawa, and W. Jastrzębski, “Theoretical and experimental study of ion-exchange process on zeolites from 5-1 structural group,” *Journal of Porous Materials*, vol. 23, no. 1, pp. 1–9, 2016, doi: 10.1007/s10934-015-0050-6.
[31] R. Dimitrijevic, V. Dondur, P. Vulic, S. Markovic, and S. Macura, “Structural characterization of pure Na-nephelines synthesized by zeolite conversion route,” *Journal of Physics and Chemistry of Solids*, vol. 65, no. 10, pp. 1623–1633, 2004, doi: 10.1016/j.jpcs.2004.03.005.
[32] B. X. Gu, L. M. Wang, and R. C. Ewing, “Effect of amorphization on the Cs ion exchange and retention capacity of zeolite-NaY,” *Journal of Nuclear Materials*, vol. 278, no. 1, pp. 64–72, 2000, doi: 10.1016/S0022-3115(99)00224-X.
[33] H. E. Kissinger, “Reaction Kinetics in Differential Thermal Analysis,” *Analytical Chemistry*, vol. 29, no. 11, pp. 1702–1706, 1957, doi: 10.1021/ac60131a045.